Design of nonlinear controller for bi-axial inverted pendulum system

L.-H. Chang and A.-C. Lee

Abstract: This study presents the use of Tustin's friction model and a disturbance observer to improve the steady-state error of a bi-axial inverted pendulum system. Then, a three-phase controller, including a swing-up control, a sliding-mode with feedback linearisation to control the angle of the pendulum, and a sliding-mode plus PID control for the pendulum-cart system is employed to eliminate the system's nonlinear and unstable characteristics. Experimental results reveal that the pendulum maximum angle of operation is $\pm 14^{\circ}$(X-axis)/$\pm 12^{\circ}$ (Y-axis); the steady-state error of the pendulum angle is $\pm 0.2^{\circ}$ (X-axis)/$\pm 0.3^{\circ}$(Y-axis), and the cart position is within ± 4 mm. Experimental results are illustrated and films are provided at the website http://midistudio.myweb.hinet.net to show the effectiveness and robustness of the proposed control schema.

1 Introduction

As in the control of a rocket, the existence of an unstable equilibrium point at the upright position and a stable equilibrium point at the pendant position of an inverted pendulum system is known as a suitable example to verify control strategies for its nonlinear open-loop unstable behaviour.

Many approaches have been applied to control inverted pendulum systems. Furuta *et al.* [1] used linear state feedback with an integrator controller to regulate a double-inverted pendulum on an inclined rail. Tsachouridis and Medrano-Cerda [2] implemented an H_{∞} controller via a robust reduced-order dynamic observer with an integrator to control a triple-inverted pendulum on an inclined rail. Some papers [3–7] performed different two-phase hybrid control algorithms to swing-up and stabilise a pendulum-cart system from the pendant position. A hammer was adopted in [6] to cause an external disturbance force to demonstrate the robustness of the system. Sprenger *et al.* [8] balanced a two-dimensional (2D, the pendulum-cart system possesses planar motion, i.e. the rod can rotate in the X–Z and Y–Z plane, instead of 1D/2 rods and 1D/3 rods) inverted pendulum on a two-joint rotational robot. They further compared the performance of three pendulum angle sensors and concluded that the encoder is the best followed by the Hall effect sensor with the potentiometer least favoured. Cho and Jung [9] presented decentralised neural networks for a circular trajectory position tracking control while balancing a two-dimensional inverted pendulum on an X–Y table. Similar to [9], Wai and Chang [10] used decentralised adaptive sliding-mode control to track a periodic sinusoidal command. However, no clear experimental data were shown. The decentralised control of [8–10] treats the coupling effects of a 2D pendulum-cart system as a disturbance. Van der Linden and Lambrechts [11] implemented an H_{∞} controller to eliminate the dry frictional force between the cart and the rail to stabilise a pendulum-cart system. Grasser *et al.* [12] built a revolutionary two-wheeled inverted pendulum that can perform stationary U-turns. Many experimental films are provided at their website to show the performance of the revolution machine. Table 1 shows the control strategies, types of pendulum and friction compensation methods used in the reference papers described above.

However, most authors have focused on control law, in either the swing-up or the stabilising region. The frictional forces that may degrade the system performance are usually ignored or treated as a bounded uncertainty. Some works consider friction compensation, but only for Coulomb and/or viscous forces. The authors' observation show that Coulomb and/or viscous friction are not the only existing forces that can cause undesirable phenomena such as stick–slip oscillation, steady-state error and poor-tracking performance.

In this study, instead of a two-phase controller as in the past, the authors propose a three-phase controller that considers cross-coupling effects. The method has advantages for the maximum angle of operation and system robustness. The overall control system shown in Fig. 1 consists of the following elements: the $\alpha\beta$-filter [13] is used to estimate the cart velocity $\dot{\mathbf{x}}$ and the pendulum angular velocity $\dot{\Theta}$; Tustin's friction model and a disturbance observer (DOB) based on the cart velocity loop are proposed to compensate for the frictional force **f** and disturbance **d** between the cart and the rail of the pendulum-cart system; the Mux block combines vector signals into a larger vector; the Demux block splits the vector signal into smaller vectors; the block of three-phase controller switching varied according to the angle of the pendulum $\boldsymbol{\Theta}$ with output force **F** is designed to eliminate the nonlinear and unstable characteristics and the three-phase control strategies involve the following (see Fig. 2):

1. Swing-up the pendulum from rest ($\pm 18^{\circ}$) to region II.
2. When the pendulum angle is in region II, the control of the position of the cart is temporarily ignored and a sliding-mode with feedback linearisation control is adopted to stabilise the angle of the pendulum. This strategy has the advantage of system robustness.

doi:10.1049/iet-cta:20060338

Paper first received 5th August and in revised form 5th December 2006

L.-H. Chang and A.-C. Lee are with the Department of Mechanical Engineering, National Chiao Tung University, 1001 Ta Hsueh Road, Hsinchu 300-10, Taiwan, Republic of China

E-mail: aclee@mail.nctu.edu.tw

Table 1: Control strategies in the references and this study

Reference	Control strategy	Pendulum dimension/ rod	Friction compensation	Photo/film
1	Linear state feedback with integrator	1D/2 rods Inclined rail	Viscous model	Photo
2	H_∞ control with integrator	1D/3 rods Inclined rail	No	No
3	Fuzzy (swing-up) and linear state feedback	1D/1 rod	No	Photo
4	Fuzzy (swing-up), adaptive sliding mode	1D/1 rod	Coulomb/bounded uncertainty	No
5	Energy approach (swing-up) and linear state feedback	1D/1 rod	No	No
6	Gray prediction (swing-up) and PD (hammer impact)	1D/1 rod	Coulomb/bounded uncertainty	Photo
7	Quasi-zero torque trajectory (swing-up) and linear-quadratic regulator (LQR) control	1D/2 rods	No	Photo/film
8	Linear state feedback (decentralised algorithm)	2D/1 rod	Coulomb + viscous model	Photo
9	Neural networks (decentralised algorithm)	2D/1 rod	No	Photo
10	Adaptive sliding-mode (decentralised algorithm)	2D/1 rod	No	No
11	H_∞ control	1D/1 rod	Coulomb/bounded uncertainty	No
12	Pole placement	1D/1 rod	No	Photo/film
This study	The three-phase control with performance specification list (9 V battery impact) (ball balancing)	2D/1 rod Inclined 15° rail (shown in film)	Coulomb + stiction + Stribeck + viscous model and DOB	Photo/film

3. When the pendulum angle is under $\pm 3^\circ$, a sliding-mode for controlling the angle of the pendulum plus a PID for controlling the position of the cart are performed to stabilise the system. The final control signals through the DAC and the motor driver with servo gain $\mathbf{K_a K_t K_n}$ are applied to control the bi-axial pendulum-cart system. The experimental results show that the proposed approach effectively controls the system.

The experimental setup of the bi-axial inverted pendulum system includes the following:

1. A cart that moves within an operation range 320×320 mm on a ball-screw-driven X–Y table, where the X-axis is on the top.

2. A pendulum with a maximum angle of inclination, $\pm 18^\circ$, is hinged on a universal joint to enable it to rotate freely in the two-dimensional working space. Two 1800-Pulse/Rev incremental optical encoders with an angular resolution of 0.05° are used to measure the angles of the pendulum.
3. Two 300 W DC motors with 1000-Pulse/Rev encoders are used as actuators to drive the cart on the X–Y table through the ball-screw. Since the pitch of the ball-screw is 5 mm, the resolution of the cart's horizontal displacement is 1.25 μm.
4. In torque mode, two motor drivers are applied to actuate the DC motors with the following specifications; maximum input voltage is ± 10 V and maximum output current is 15 A (transient) and 5 A (continuous).
5. A 4-axis motion control card is connected between a PC and the pendulum-cart system to record the angles of the

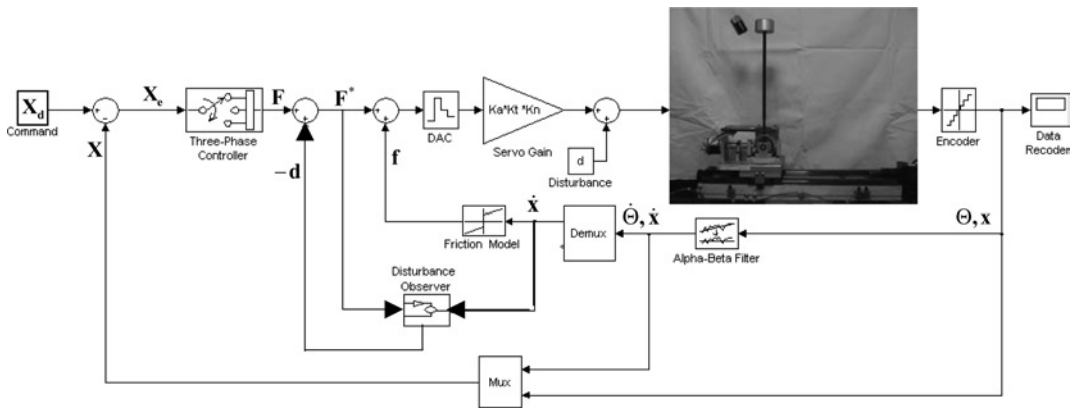

Fig. 1 *Whole control loop of the bi-axial inverted pendulum system*

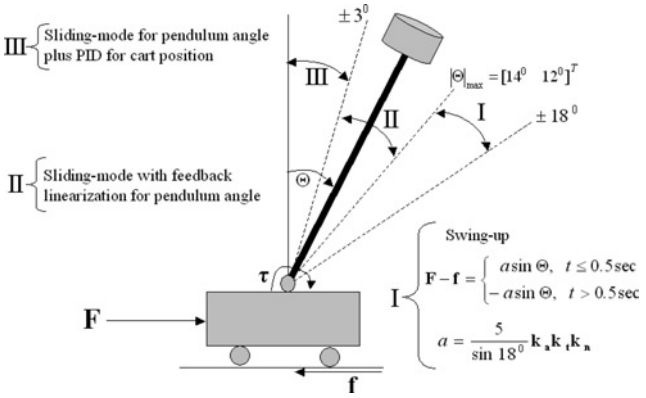

Fig. 2 *Three-phase controller, switching varied according to the angle of the pendulum*

pendulum and the positions of the cart, and to send DAC signals to the motor drivers.

6. The host computer was an AMD K6-2 500 MHz PC and the control algorithm was written in Borland C++ 3.1 with a sampling rate of 500 Hz.

2 System modelling

The two-dimensional inverted pendulum system, as shown in Fig. 3, is adopted to formulate the equations of motion. Tables 2 and 3 are the nomenclature and values of the real system. The equations of motion can be obtained by using the Euler-Lagrange formulation as follows

$$\begin{bmatrix} \ddot{x} \\ \ddot{y} \end{bmatrix} = \begin{bmatrix} c_3c_0 & -c_3c_1 \\ -\bar{c}_3\bar{c}_1 & \bar{c}_3\bar{c}_0 \end{bmatrix} \begin{bmatrix} (F_x - f_x) \\ (F_y - f_y) \end{bmatrix} + \begin{bmatrix} c_3c_2 \\ \bar{c}_3\bar{c}_2 \end{bmatrix} \quad (1)$$

$$\begin{bmatrix} \ddot{\theta} \\ \ddot{\phi} \end{bmatrix} = \begin{bmatrix} -c_4c_6c_3c_0 & c_4c_6c_3c_1 \\ \bar{c}_4\bar{c}_6\bar{c}_3\bar{c}_1 & -\bar{c}_4\bar{c}_6\bar{c}_3\bar{c}_0 \end{bmatrix} \begin{bmatrix} (F_x - f_x) \\ (F_y - f_y) \end{bmatrix} + \begin{bmatrix} -c_4c_6c_3c_2 + c_4c_5 - c_4\tau_\theta \\ -\bar{c}_4\bar{c}_6\bar{c}_3\bar{c}_2 + \bar{c}_4\bar{c}_5 - \bar{c}_4\tau_\phi \end{bmatrix} \quad (2)$$

where

$$k_{0x} = m_{0x} + m_1 + m_2$$
$$k_{0y} = m_{0y} + m_1 + m_2$$
$$k_1 = m_1l_1 + m_2l_2$$
$$k_2 = J_1 + J_2 + m_1l_1^2 + m_2l_2^2$$

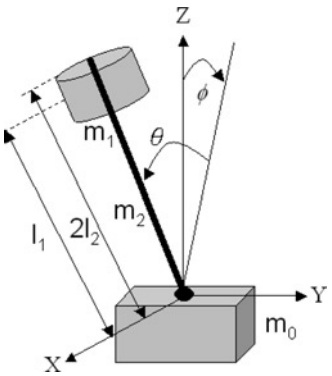

Fig. 3 *Coordination of the two-dimensional inverted pendulum*

$$\Delta_x = k_{0x}k_2 - k_1^2\cos^2\theta$$
$$\Delta_y = k_{0y}k_2 - k_1^2\cos^2\phi$$
$$c_0 = k_2\Delta_y\cos\phi$$
$$c_1 = k_1^2k_2\cos^2\phi\sin\phi\sin\theta$$
$$c_2 = k_1\Delta_y\cos\theta\cdot\tau_\theta - k_{0y}k_1k_2\cos\phi\sin\phi\sin\theta\cdot\tau_\phi + k_1k_2\Delta_y\cos\phi[\cos\phi\sin\theta(\dot{\theta}^2 + \dot{\phi}^2) + 2\dot{\theta}\dot{\phi}\sin\phi \times\cos\theta] + k_{0y}k_1k_2\cos\phi\sin^2\phi\sin\theta(k_1g\cos\theta - k_2\dot{\theta}^2\cos\phi) - k_1^3k_2\cos^2\phi\sin^2\phi\sin\theta\dot{\phi}^2 - k_1\Delta_y\cos\phi\cos\theta(k_1g\sin\theta + 2k_2\dot{\phi}\dot{\theta}\sin\phi)$$
$$c_3 = (\Delta_x\Delta_y\cos\phi - k_{0y}k_1^2k_2\cos\phi\sin^2\phi\sin^2\theta)^{-1}$$
$$c_4 = (k_2\cos\phi)^{-1}$$
$$c_5 = k_1g\sin\theta + 2k_2\dot{\phi}\dot{\theta}\sin\phi$$
$$c_6 = k_1\cos\theta$$

and $\bar{c}_i$ can be obtained by interchanging (x, θ) with (y, ϕ) in c_i, i.e.

$$\bar{c}_0 = k_2\Delta_x\cos\theta$$
$$\bar{c}_1 = k_1^2k_2\cos^2\theta\sin\theta\sin\phi$$
$$\bar{c}_2 = k_1\Delta_x\cos\phi\cdot\tau_\phi - k_{0x}k_1k_2\cos\theta\sin\theta\sin\phi\cdot\tau_\theta + k_1k_2\Delta_x\cos\theta[\cos\theta\sin\phi(\dot{\phi}^2 + \dot{\theta}^2) + 2\dot{\phi}\dot{\theta}\sin\theta \times\cos\phi] + k_{0x}k_1k_2\cos\theta\sin^2\theta\sin\phi(k_1g\cos\phi - k_2\dot{\phi}^2\cos\theta) - k_1^3k_2\cos^2\theta\sin^2\theta\sin\phi\dot{\theta}^2 - k_1\Delta_x\cos\theta\cos\phi(k_1g\sin\phi + 2k_2\dot{\theta}\dot{\phi}\sin\theta)$$
$$\bar{c}_3 = (\Delta_y\Delta_x\cos\theta - k_{0x}k_1^2k_2\cos\theta\sin^2\theta\sin^2\phi)^{-1}$$
$$\bar{c}_4 = (k_2\cos\theta)^{-1}$$
$$\bar{c}_5 = k_1g\sin\phi + 2k_2\dot{\theta}\dot{\phi}\sin\theta$$
$$\bar{c}_6 = k_1\cos\phi$$

The following symbols are defined as

$$\mathbf{x} = [x \quad y]^{\mathrm{T}}, \quad \boldsymbol{\Theta} = [\theta \quad \phi]^{\mathrm{T}}, \quad \mathbf{F} = [F_x \quad F_y]^{\mathrm{T}},$$
$$\mathbf{f} = [f_x \quad f_y]^{\mathrm{T}},$$
$$\boldsymbol{\tau} = [\tau_\theta \quad \tau_\phi]^{\mathrm{T}}, \mathbf{X_d} = \begin{bmatrix} \theta_d & \dot{\theta}_d & x_d & \dot{x}_d \\ \phi_d & \dot{\phi}_d & y_d & \dot{y}_d \end{bmatrix}^{\mathrm{T}},$$
$$\mathbf{X} = \begin{bmatrix} \theta & \dot{\theta} & x & \dot{x} \\ \phi & \dot{\phi} & y & \dot{y} \end{bmatrix}^{T}$$

From (1), (2), it is observed that the frictional force **f** and the joint frictional torque $\boldsymbol{\tau}$ will degrade the performance of the pendulum-cart system.

3 Tustin's friction model and the disturbance observer

The static Tustin friction model [14, 15] and the disturbance observer [16, 17] are employed to compensate for the friction and disturbance between the cart and the rail. Tustin's model, shown in Fig. 4, comprises Coulomb force, stiction

Table 2: Nomenclature

Symbol	Description
x/y	position of the cart at the X/Y axis
θ/ϕ	angle of pendulum about the X/Y direction
F_x/F_y	control force on the X/Y axis
f_x/f_y	frictional force on the X/Y axis
τ_θ/τ_ϕ	joint frictional torque in the θ/ϕ direction
m_{0x}/m_{0y}	cart mass of X/Y axis
m_1	pendulum head mass
m_2	rod mass
$m_{eq} = m_1 + m_2$	equivalent mass of the pendulum
M	the summation of the cart mass and m_{eq}
l_1	length of the pendulum from the head to the cart
l_2	half-length of the rod
l_{eq}	equivalent length of the pendulum
r_1	radius of the pendulum head
r_2	rod radius
r_{joint}	bearing radius of the joint
J_1	moment of inertia of the pendulum head with respect to the cart
J_2	moment of inertia of the rod with respect to the cart
K_a	motor driver gain
K_t	motor torque constant
K_n	ballscrew transfer factor
$K_aK_tK_n$	servo gain
K_p	gain
T_d	Coulomb force between the cart and the rail
T_h	stiction force between the cart and the rail
v_s	Stribeck velocity constant
v	cart velocity
B	viscous damping coefficient between the cart and the rail
j_{b_x}/j_{b_y}	joint viscous damping coefficient in the X/Y direction
j_{c_x}/j_{c_y}	joint Coulomb force in the X/Y direction

force, Stribeck force and viscous force and is expressed as follows

$$f = T_d + (T_h - T_d)\mathrm{e}^{-(v/v_s)} + Bv \tag{3}$$

In Tustin's model, the schema shown in Fig. 5 is used to establish the friction-velocity map. Since steady-state velocity is concerned with obtaining the friction-velocity map, the effect of phase shift induced by a digital-to-analogue converter (DAC), encoder and $\alpha\beta$-filter is negligible in the case. When the system's velocity response v reaches a steady state, i.e. $v = v_{ss}$, the input force to the pendulum-cart is equivalent to the frictional force. Fig. 5 equals the following

$$Bv_{ss} + T_f = K_pK_aK_tK_n(u - v_{ss}) \tag{4}$$

where $T_f = T_d + (T_h - T_d)\mathrm{e}^{(-v/v_s)}$.

Varying the step command u from low velocity to high velocity yields the force set $K_pK_aK_tK_n(u - v_{ss})$ and the pendulum-cart velocity response set v_{ss}. Meanwhile, the stiction force is obtained by using the open-loop breakaway

Table 3: Parameters of the real system

m_{0x}	3.1 kg
m_{0y}	14.2 kg
m_1	0.25 kg
m_2	0.05 kg
m_{eq}	0.3 kg
l_1	0.32 m
l_2	0.1675 m
l_{eq}	0.2946 m
r_1	0.025 m
r_2	0.004 m
r_{joint}	0.0045 m
J_1	8.6×10^{-3} kg · m^2
J_2	4.68×10^{-4} kg · m^2
K_t	2.65 kg · cm/A
K_n	Force/Torque $= 2\pi/0.005$
$K_aK_tK_n$	2.3 N/V (X-axis); 10.57 N/V (Y-axis)
K_p	1.5

test. A voltage increase of $2^{-14}\,V/s$ is applied to the pendulum-cart system. The T_h is obtained from the abrupt change in the pendulum-cart position response with the threshold set at two encoder counts. Fig. 6 plots the friction-velocity experimental data. The parameters of Tustin's friction model for both axes are obtained by using the least-square method. The equations are as follows:

$$f_x \begin{cases} f_{v_x^+} = [0.4151 + (0.54 - 0.4151)\mathrm{e}^{-(v_x^+/738.9)} \\ \qquad +11.1871v_x^+] \\ f_{v_x^-} = -[0.4701 + (0.55 - 0.4701)\mathrm{e}^{-(|v_x^-|/839.2)} \\ \qquad +12.976|v_x^-|] \end{cases} \quad \text{N (5a)}$$

$$f_x \begin{cases} f_{v_y^+} = [1.7789 + (2.4311 - 1.7789)\mathrm{e}^{-(v_y^+/3662.5)} \\ \qquad +54.7558v_y^+] \\ f_{v_y^-} = -[2.116 + (2.9596 - 2.116)\mathrm{e}^{-(|v_y^-|/4094.1)} \\ \qquad +68.5919|v_y^-|] \end{cases} \quad \text{N(5b)}$$

In relation to the pendulum joint friction, the Stribeck force cannot be experimentally observed, only the viscous force and Coulomb force are considered. The parameters are obtained by comparing the experimental data on the

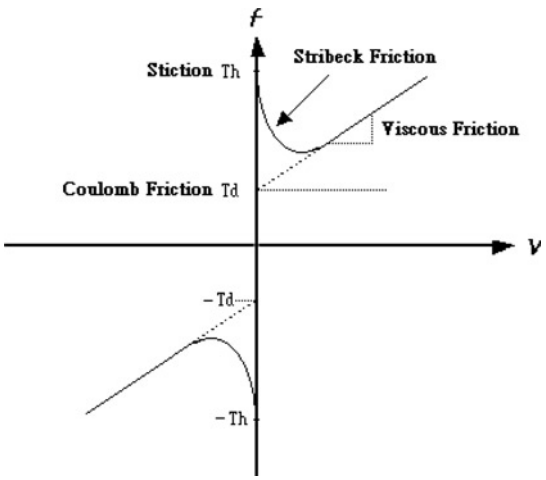

Fig. 4 *Tustin's friction model*

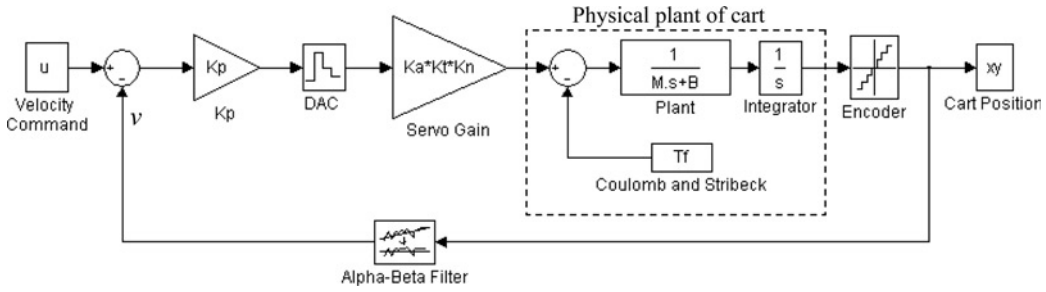

Fig. 5 *Control schema used in constructing Tustin's friction model*

natural oscillation of the pendulum with the following equation

$$\ddot{\Theta} + \frac{r_{\text{joint}}^2}{l_{\text{eq}}^2 m_{\text{eq}}}\mathbf{j_b}\dot{\Theta} + \frac{g}{l_{\text{eq}}}\sin\Theta - \frac{r_{\text{joint}}}{l_{\text{eq}}^2 m_{\text{eq}}}\mathbf{j_C}\,\text{sgn}(\dot{\Theta}) = 0 \quad (6)$$

where $\mathbf{j_b} = [j_{b_x} \quad j_{b_y}]^{\text{T}}$, $\mathbf{j_C} = [j_{C_x} \quad j_{C_y}]^{\text{T}}$. The $\mathbf{j_b}$ and $\mathbf{j_C}$ are obtained as follows

$$\mathbf{j_b} = [45 \quad 30]^{\text{T}}\ \text{kg/s}, \quad \mathbf{j_C} = [0.168 \quad 0.168]^{\text{T}}\ \text{N}$$

Since the frictional force of the physical plant depends on time, temperature, the position of the cart and other factors. The static Tustin's friction model cannot exactly model the frictional force at all times. Moreover, external disturbances and plant uncertainties will degrade the performance of the system. For the cart velocity feedback loop system, the DOB shown in Fig. 7 is employed to solve this problem. In Fig. 7, the $\mathbf{P(s)} = \mathbf{K_a K_t K_n}/(\mathbf{Ms} + \mathbf{B})$ denotes the transfer function of cart model including the servo gain between cart velocity command and response; $\mathbf{P_n(s)}$ is nominal plant of $\mathbf{P(s)}$; $\mathbf{d}$ is disturbance; $\boldsymbol{\varsigma}(\mathbf{s})$ is measurement noise. A DOB is generally introduced into motion control systems to eliminate the 'equivalent disturbance' as much as possible, and to force the actual system to become a nominal plant. The details of how a DOB works have been explained elsewhere [16, 17]. In DOB, $\mathbf{Q(s)}$ can be interpreted as a complementary sensitivity function. Therefore, a sensible choice is to let the low frequency dynamics of $\mathbf{Q(s)}$ close to one for disturbance rejection and model uncertainties. In this study, a second-order Butterworth lowpass filter (LPF) [18]

$$\mathbf{Q(s)} = \frac{1}{(\mathbf{s}/\mathbf{w_c})^2 + \sqrt{2}(\mathbf{s}/\mathbf{w_c}) + 1} \quad (7)$$

is designed so that the equation $\mathbf{Q(s)}/\mathbf{P_n(s)}$ in DOB is a strict proper function. The cutoff frequency $\mathbf{w_c}$ is designed at 100 Hz and the zero-order hold (ZOH) equivalence of the analogue filter is used to determine the digital Butterworth LPF $\mathbf{Q(z)}$ with a sampling rate of 500 Hz. Since the closed-loop system bandwidth of the pendulum-cart system is around 3 rad/s in our study, the difference of phase shift between a continuous LPF and the digital one is negligible. The parameters of $\mathbf{Q(z)}$, $\mathbf{P_n(s)}$ and $(\mathbf{Q}/\mathbf{P_n})(\mathbf{z})$ are listed in Table 4. Therefore, the DOB output $-\mathbf{d(z)}$ is obtained as

$$-\mathbf{d(z)} = \left[\mathbf{Q(z)}\mathbf{F}^* - \frac{\mathbf{Q}}{\mathbf{P_n}}(\mathbf{z})\dot{\mathbf{x}}\right] \quad \text{N} \quad (8)$$

4 Design of control law

In this section, Tustin's friction model and the DOB are assumed to compensate for the friction and disturbance between the cart and the rail. The three-phase controller,

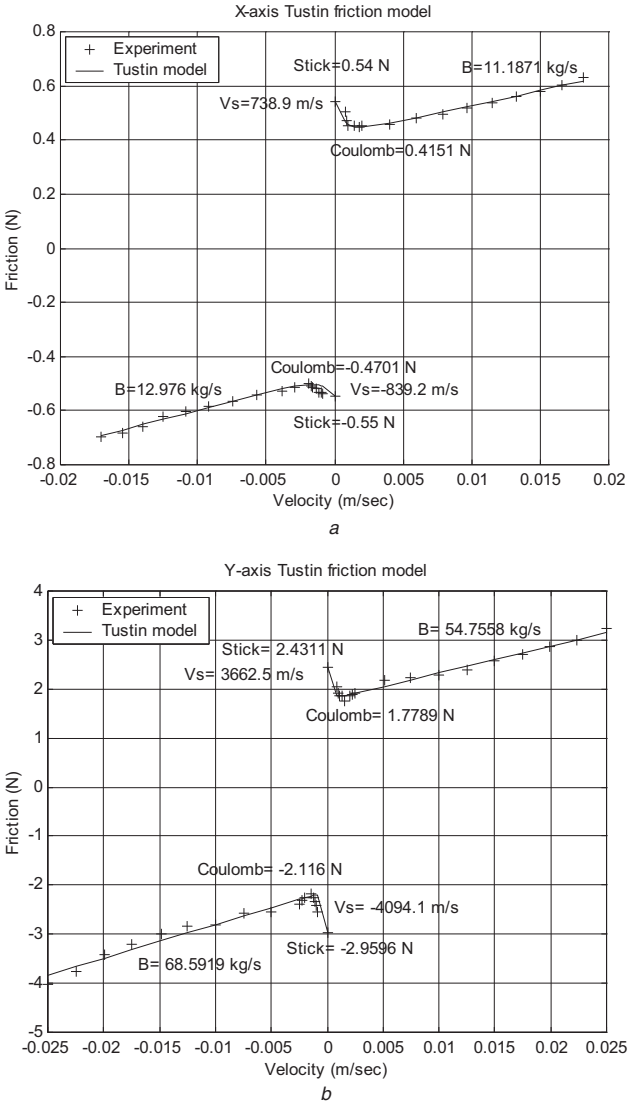

Fig. 6 *Friction-velocity map for the two axes*
a X-axis
b Y-axis

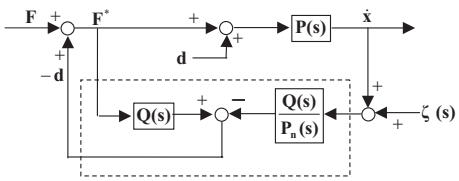

Fig. 7 *DOB structure (dashed line)*

Table 4: Parameters of DOB

Q(z)	$P_n(s)$	$\frac{Q}{P_n}(z)$
$\frac{0.4215z^{-1}+0.229z^{-2}}{1-0.5186z^{-1}+0.1691z^{-2}}$	$P_{nx}(s)=\frac{2.3}{3.4s+12}$	$\frac{Q}{P_{nx}}(z)=\frac{421.4768z^{-1}-418.083z^{-2}}{1-0.5186z^{-1}+0.1691z^{-2}}$
	$P_{ny}(s)=\frac{10.57}{14.5s+61.68}$	$\frac{Q}{P_{ny}}(z)=\frac{391.54z^{-1}-387.75z^{-2}}{1-0.5186z^{-1}+0.1691z^{-2}}$

switched according to the pendulum angle Θ, is designed to cope with the bi-axial pendulum-cart system. The control strategies involve the following:

Region I: Swing-up control.
When the pendulum rests at $\pm 18^\circ$, the cart is accelerated for a short time and then pushed back immediately to erect the pendulum into region II. The swing-up algorithm is

$$\mathbf{F}=\begin{cases} a\sin\Theta, t\le 0.5\,\mathrm{s} \\ -a\sin\Theta, t>0.5\,\mathrm{s}\end{cases} \text{ where } a=\frac{5}{\sin 18^\circ}K_aK_tK_n \quad (9)$$

Region II: Sliding-mode with feedback linearisation control for the angle of the pendulum.

When the angle of the pendulum is in region II, the control of the position of the cart is temporarily ignored and will be reactuated in region III. A sliding-mode [19, 20] with feedback linearisation control is implemented to ensure the erection of the pendulum and to drive the angle of the pendulum into region III. The control strategy provides the advantages of maximised operation angle of the pendulum and system robustness. The control law in this region is

$$\mathbf{F}=-\begin{bmatrix} -c_4c_6c_3c_0 & c_4c_6c_3c_1 \\ \bar{c}_4\bar{c}_6\bar{c}_3\bar{c}_1 & -\bar{c}_4\bar{c}_6\bar{c}_3\bar{c}_0\end{bmatrix}^{-1} \times\begin{bmatrix} -c_4c_6c_3c_2+c_4c_5-c_4\tau_\theta+(k_{\dot\theta}\dot\theta+k_\theta\theta-u_x) \\ -\bar{c}_4\bar{c}_6\bar{c}_3\bar{c}_2+\bar{c}_4\bar{c}_5-\bar{c}_4\tau_\phi+(k_{\dot\phi}\dot\phi+k_\phi\phi-u_y)\end{bmatrix} \quad (10)$$

Setting $\mathbf{k}_\Theta=[k_\theta \quad k_\phi]^T$ and $\mathbf{k}_{\dot\Theta}=[k_{\dot\theta} \quad k_{\dot\phi}]^T$ as positive definite and substituting (10) into (2) yields

$$\ddot\Theta+\mathbf{k}_{\dot\Theta}\dot\Theta+\mathbf{k}_\Theta\Theta=\left(\frac{\mathbf{d}}{\mathbf{dt}}+\boldsymbol{\lambda}_1\right)\left(\frac{\mathbf{d}}{\mathbf{dt}}+\boldsymbol{\lambda}_2\right)\Theta =\mathbf{u}+\mathbf{e_0} \quad (11)$$

where $\boldsymbol{\lambda}_\mathbf{i}>0$, $\mathbf{u}=[u_x \quad u_y]^T$, and $\mathbf{e_0}$ denotes the uncertainties of the system such as the measurement error of the pendulum angle Θ and the estimation error of $\dot\Theta$ determined using the $\alpha\beta$-filter. In this study, the sliding surface is taken as

$$\mathbf{s}=[s_x \quad s_y]^T=\left(\frac{\mathbf{d}}{\mathbf{dt}}+\boldsymbol{\lambda}_2\right)\Theta \quad (12a)$$

and the switching force

$$\mathbf{u}=-\gamma\,\mathrm{sgn}(\mathbf{s}) \quad (12b)$$

where $\gamma>||\mathbf{e_0}||$.

Substituting (12) into (11) and multiplying by $\mathbf{s}^T$ yields

$$\mathbf{s}^T(\dot{\mathbf{s}}+\boldsymbol{\lambda}_1\mathbf{s})=-\gamma|\mathbf{s}|+\mathbf{s}^T\mathbf{e_0}<0 \quad (13)$$

Since $\mathbf{s}^T\boldsymbol{\lambda}_1\mathbf{s}>0$, therefore $\mathbf{s}^T\dot{\mathbf{s}}<0$, $\forall\mathbf{s}\neq 0$.

Equation (11) is asymptotically stable. The pendulum angle can reach the sliding surface in a limited time and slide toward the desired state $\Theta=0$. In this study, the sliding-mode gains $\mathbf{k}_\Theta$ and $\mathbf{k}_{\dot\Theta}$, the value of $\boldsymbol{\lambda}_\mathbf{i}$ and the sliding surface $\mathbf{s}$ are listed in Table 5.

Region III: Sliding-mode for controlling the angle of the pendulum plus PID for controlling the position of the cart.

In this region, the controls for the pendulum angle and the cart position are considered simultaneously to stabilise the bi-axial pendulum-cart system. The control law is designed as

$$\mathbf{F}=-\begin{bmatrix} -c_4c_6c_3c_0 & c_4c_6c_3c_1 \\ \bar{c}_4\bar{c}_6\bar{c}_3\bar{c}_1 & -\bar{c}_4\bar{c}_6\bar{c}_3\bar{c}_0\end{bmatrix}^{-1} \times\begin{bmatrix} -c_4c_6c_3c_2+c_4c_5-c_4\tau_\theta+(k_{\dot\theta}\dot\theta+k_\theta\theta-D_x(x_e,\dot x_e)-u_x) \\ -\bar{c}_4\bar{c}_6\bar{c}_3\bar{c}_2+\bar{c}_4\bar{c}_5-\bar{c}_4\tau_\phi+(k_{\dot\phi}\dot\phi+k_\phi\phi-D_y(y_e,\dot y_e)-u_y)\end{bmatrix} \quad (14)$$

where $D_x(x_e,\dot x_e)=k_{p_x}x_e+k_{d_x}\dot x_e+\int k_{i_x}\,\mathrm{d}x_e$ and $D_y(y_e,\dot y_e)=k_{p_y}y_e+k_{d_y}\dot y_e+\int k_{i_y}\,\mathrm{d}y_e$.

Let

$$\mathbf{D}(\mathbf{x_e},\,\dot{\mathbf{x}}_\mathbf{e})=(\mathbf{k_p}\mathbf{x_e}+\mathbf{k_d}\dot{\mathbf{x}}_\mathbf{e}+\int\mathbf{k_i}\,\mathbf{dx_e}) \quad (15)$$

where $\mathbf{D}(\mathbf{x_e},\,\dot{\mathbf{x}}_\mathbf{e})=[D_x(x_e,\,\dot x_e) \quad D_y(y_e,\,\dot y_e)]^T$. Substituting (14) into (2) yields

$$\ddot\Theta+\mathbf{k}_{\dot\Theta}\dot\Theta+\mathbf{k}_\Theta\Theta=\mathbf{u}+\mathbf{e_0}+\mathbf{D}(\mathbf{x_e},\,\dot{\mathbf{x}}_\mathbf{e}) \quad (16)$$

The PID gains of $\mathbf{D}(\mathbf{x_e},\,\dot{\mathbf{x}}_\mathbf{e})$ should be selected such that its effects on the pendulum angle can be eliminated by the switching force of the sliding-mode

$$\mathbf{u}=-\gamma\,\mathrm{sgn}(\mathbf{s}) \quad (17)$$

where $\gamma>||\mathbf{e_0}+\mathbf{D}(\mathbf{x_e},\,\dot{\mathbf{x}}_\mathbf{e})||$.

Therefore, the pendulum angle can be kept in the sliding surface when the cart position control is reactuated in this region. Concerning the sliding-mode chattering, a boundary layer will reduce chattering along the manifold but will also

Table 5: Control parameters of region II

$\mathbf{k}_\Theta$	$\mathbf{k}_{\dot\Theta}$	$\boldsymbol{\lambda}_\mathbf{i}$	$\mathbf{s}$
$[254.5 \quad 145.6]^T$	$[32.02 \quad 24.3]^T$	$(-17.3 \quad -14.7)$/X-axis $(-13.5 \quad -10.8)$/Y-axis	$[\dot\theta+14.7\theta \quad \dot\phi+10.8\phi]^T$

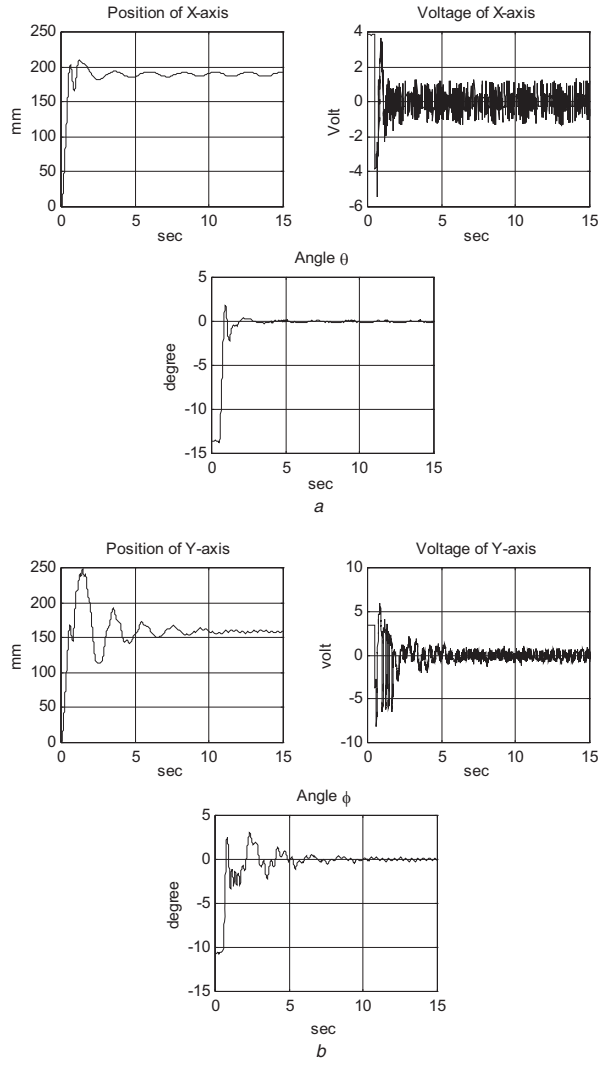

Fig. 8 *Bi-axial control performance by the three-phase controller*
a Position, angle and control about the X-axis
b Position, angle and control about the Y-axis

reduce the control performance. In our study, the experiments were performed once using a boundary layer, but the performance deteriorated. Therefore, results without using a boundary layer are presented and furthermore, for the underlying system, the chattering can be tolerated and

Table 6: Comparison of steady-state error among several compensation strategies

Control strategy	$\lvert\theta_e\rvert_{\max}$	$\lvert x_e\rvert_{\max}$
Three-phase control + DOB + Tustin's model (this study)	0.2°	4
Three-phase control	1.2°	31 mm
Three-phase control + DOB	1.1°	27 mm
Three-phase control + Tustin's	0.3°	6.5 mm
Three-phase control + (Tustin's – Coulomb)	1.0°	22.5 mm
Three-phase control + (Tustin's – viscous)	1.1°	26 mm
Three-phase control + (Tustin's – Stribeck)	0.4°	9 mm

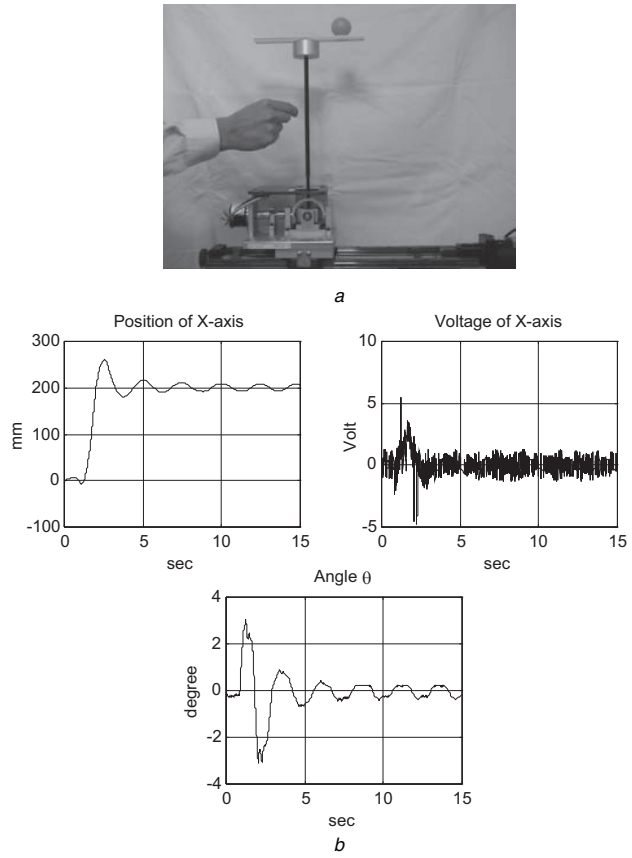

Fig. 9 *Experimental photograph and data on rapid shift of the pendulum-cart system*
a Experimental photograph
b Experimental data

the system performs well. Since the PID gains are incorporated in the sliding-mode control loop, the tuning is a compromise between the switching gain γ and the performance of the cart position. The values are set to $\gamma = 0.5$, $\mathbf{k_p} = [60 \quad 52]^{\mathrm{T}}$, $\mathbf{k_d} = [20 \quad 14]^{\mathrm{T}}$ and a small integral gain $\mathbf{k_i} = \mathbf{k_p}/1000$. Herein, $\mathbf{D}(\mathbf{x_e}, \dot{\mathbf{x}}_\mathbf{e})$ and $\mathbf{e_0}$ are estimated to be 0.4 and 0.003, respectively. Substituting the feedback gains $\mathbf{k}_\Theta$, $\mathbf{k}_{\dot{\Theta}}$, $\mathbf{k_p}$ and $\mathbf{k_d}$ into the linearised pendulum-cart system yields the eigenvalues of X-axis and Y-axis as$(-8.85 \pm 7.61i \quad -0.338 \pm 1.79i)$ and $(-7.05 \pm 3.46i \quad -0.129 \pm 2.52i)$. The zeros of the two axes are the same, ± 4.9, revealing that the system is a non-minimum phase system.

Substituting (14) into (1) yields

$$\begin{bmatrix} \ddot{x} + \frac{1}{c_4 c_6}[D_x(x_e, \dot{x}_e) - (k_{\dot{\theta}}\dot{\theta} + k_\theta\theta - u_x)] - \frac{1}{c_6}(c_5 - \tau_\theta) \\ \ddot{y} + \frac{1}{\bar{c}_4 \bar{c}_6}[D_y(y_e, \dot{y}_e) - (k_{\dot{\phi}}\dot{\phi} + k_\phi\phi - u_y)] - \frac{1}{\bar{c}_6}(\bar{c}_5 - \tau_\phi) \end{bmatrix} = 0 \tag{18}$$

When the pendulum angle reaches the sliding surface and slides toward $\Theta = 0$, the pendulum-cart system is obtained as

$$\ddot{\mathbf{x}} + \frac{k_2}{k_1}(\mathbf{k_p}\mathbf{x_e} + \mathbf{k_d}\dot{\mathbf{x}}_\mathbf{e} + \int \mathbf{k_i}\mathbf{dx_e}) + \frac{r_{\text{joint}}}{k_1}\mathbf{j_C} + \mathbf{e_1} = 0 \tag{19}$$

where $\mathbf{e_1} = (18) - (18)|_{\Theta=\dot{\Theta}=\mathbf{0}}$. Eq. (19) reveals that the system's steady-state error induced by both $\mathbf{j_C}$ and $\mathbf{e_1}$ could be suppressed by the small integral gain $\mathbf{K_i}$.

5 Experimental results

In software design, the values of Tustin's friction model $\mathbf{f}$, the DOB output $-\mathbf{d}$ and the control force $\mathbf{F}$ described in the previous sections should be divided by the servo gain $\mathbf{K_a K_t K_n}$. Fig. 8 plots the experimental data of the bi-axial three-phase control with friction compensation and DOB (Film: Pendulum_Precision). Table 6 summarises the control performance of the X-axis for several compensation strategies. The results show that the control strategy proposed is the best, which improves the control performance more than six times as compared to the method of no compensation. Moreover, compensation for the viscous force is more important than for the Coulomb force. Notably, the Stribeck force compensation also contributes to the performance of the system (Film: Friction_Cmp_OX). The following experiments were conducted to verify that the proposed control schema ensured the system stability and robustness:

1. Maximum operation angle (MOA) test: The MOA is an important performance index for the three-phase controller. In this experiment, the swing-up control in region I is temporarily inactive. The operation angle to trigger the controller in region II is varied from $|\Theta| = 10^\circ$ to $|\Theta| = 18^\circ$. The rod is slowly pushed from rest to an angle Θ. When the pendulum rod reaches angle Θ, a small force is applied to the rod to push it into region II and to determine whether the pendulum is erect. This procedure is repeated on the X-axis/Y-axis. The MOA is obtained $|\Theta|_{\max} = [14^\circ \quad 12^\circ]^{\mathrm{T}}$ (Film: Max_Operation_Angle_Test). Moreover, if only the region III is active, MOA is $|\Theta|_{\max} = [7^\circ \quad 6^\circ]^{\mathrm{T}}$.
2. Robustness test for system in region II: Fig. 9*a* shows two 200 mm-long plastic tubes glued in parallel on top of the pendulum. When the pendulum is in a steady state, a ping-pong ball is placed on the two tubes. A 200 mm rapid shift is performed. The experimental data plotted in Fig. 9*b* demonstrates that when the angle of the pendulum reaches $|\theta| = 3^\circ$ from region III, the control strategy switches to region II control, and then the pendulum is pushed back to region III. Therefore, the three-phase controller, especially that in region II, has important advantages of system stability and robustness. Additionally, the non-minimum phase phenomenon of the cart position occurs at 1.1 s in the sub-figure, 'Position of X-axis', of Fig. 9*b* (Film: X_Ball_RapidShift_Impact).
3. A 9 V battery is used to impact the pendulum head to verify the robustness of the system (see Fig. 1 and Film: Bi-Axis_Impact).

6 Conclusions

In this study, Tustin's friction model and the disturbance observer are applied to compensate for friction and disturbance between a cart and a rail. Then, a three-phase controller, switched according to the angle of the pendulum, was proposed to swing-up and stabilise the pendulum-cart system. The experimental results show that the proposed approach effectively controls the bi-axial inverted pendulum system. An interesting finding is that the control strategy in region II, by stabilising only the angle of the pendulum, provides important advantages of system stability and robustness. Many films are provided at the website http://midistudo.myweb.hinet.net to demonstrate the system's stability and robustness.

7 References

1 Furuta, K., Kajiwara, H., and Kosuge, K.: 'Digital control of a double inverted pendulum on an inclined rail', *Int. J. Control*, 1980, **32**, (5), pp. 907–924
2 Tsachouridis, V.A., and Medrano-Cerda, G.A.: 'Discrete-time H_∞ control of a triple inverted pendulum with single control input', *IEE Proc., Control Theory Appl.*, 1999, **146**, (6), pp. 567–577
3 Lin, C.E., and Sheu, Y.R.: 'A hybrid-control approach for pendulum-car control', *IEEE Trans. Indus. Electron.*, 1992, **39**, (3), pp. 208–214
4 Chen, C.S., and Chen, W.L.: 'Robust adaptive sliding-mode control using fuzzy modeling for an inverted-pendulum system', *IEEE Trans. Indus. Electron.*, 1998, **45**, (2), pp. 297–306
5 Lozano, R., Fantoni, I., and Block, D.J.: 'Stabilization of the inverted pendulum around its homoclinic orbit', *Systems & Control Lett.*, 2000, **40**, pp. 197–204
6 Huang, S.J., and Huang, C.L.: 'Control of an inverted pendulum using grey prediction model', *IEEE Trans. Indus. Applic.*, 2000, **36**, (2), pp. 452–458
7 Rubi, J., Rubio, A., and Avello, A.: 'Swing-up control problem for a self-erecting double inverted pendulum', *IEE Proc., Control Theory Appl.*, 2002, **149**, (2), pp. 169–175
8 Sprenger, B., Kucera, L., and Mourad, S.: 'Balancing of an inverted pendulum with a SCARA robot', *IEEE/ASME Trans. Mechatronics*, 1998, **3**, (2), pp. 91–97
9 Cho, H.T., and Jung, S.: 'Balancing and position tracking control of an inverted pendulum on an X-Y plane using decentralized neural networks'. Proc. IEEE/ASME Int. Conf. on Advanced Intelligent Mechatronics (AIM2003), 2003, pp. 181–186
10 Wai, R.J., and Chang, L.J.: 'Adaptive stabilizing and tracking control for a nonlinear inverted-pendulum system via sliding-mode technique', *IEEE Trans. Indus. Electron.*, 2006, **53**, (2), pp. 674–692
11 van der Linden, G.W., and Lambrechts, P.F.: 'H_∞ control of an experimental inverted pendulum with dry friction', *IEEE Control Syst. Mag.*, 1993, **13**, (4), pp. 44–50
12 Grasser, F., D'Arrigo, A., Colombi, S., and Rufer, A.C.: 'JOE: A mobile, inverted pendulum', *IEEE Trans. Indus. Electron.*, 2002, **49**, (1), pp. 107–114
13 Edward, P.C.: 'Digital filtering: an introduction' (Houghton Mifflin Co., Boston, 1992)
14 Tustin, A.: 'The effects of backlash and of speed-dependent friction on the stability of closed-cycle control systems', *IEE J.*, 1947, **94**, (2A), pp. 143–151
15 Armstrong-Hélouvry, B., Dupont, P., and Canudas de Wit, C.: 'A survey of models, analysis tools and compensation methods for the control of machines with friction', *Automatica*, 1994, **30**, (7), pp. 1083–1138
16 Umeno, T., and Hori, Y.: 'Robust speed control of DC servomotors using modern two degree-of-freedom controller design', *IEEE Trans. Indus. Electron.*, 1991, **38**, (5), pp. 363–368
17 Lee, H.S., and Tomizuka, M.: 'Robust motion controller design for high-accuracy positioning systems', *IEEE Trans. Indus. Electron.*, 1996, **43**, (1), pp. 48–55
18 Millman, J.: 'Microelectronics: digital and analog circuits and systems' (McGraw-Hill, New York, 1979)
19 Slotine, J.-J.E., and Li, W.: 'Applied nonlinear control' (Prentice-Hall, New Jersey, 1991)
20 Khalil, H.K.: 'Nonlinear systems' (Prentice-Hall, New Jersey, 2000)